Reviews of Electromagnetics, Vol. IV, 2025
EuCAP 2025 Special Issue
DOI: 10.53792/RoE/2025/25018

Reviews of Electromagnetics
EuCAP 2025 Special Issue

Wideband Filtering Patch Antenna Design for cmWave 6G Applications

Duy Hai Nguyen[1], Martin Jacob[1], Arslan Azhar[1], Thomas Käubler[1]

Abstract
This paper presents a dual-polarized planar patch antenna design for 6G applications in the cmWave frequency band. The antenna is fabricated using a low-cost, low-loss multilayer RF laminate, achieving a radiation efficiency of 92%. A wide impedance bandwidth of 20% is realized through differential L-probe feeds. To suppress unwanted radiation in the mmWave band (24.25–27.5 GHz), shorting pins are introduced at the feed structure. The antenna's performance is validated through measurements, including radiation pattern characteristics and a practical demonstration of analog beam steering using a Butler matrix. Furthermore, a post-processing technique is discussed to filter unwanted radiation artifacts caused by measurement setups, enabling more accurate far-field characterization.

Key terms
6G, cmWave, patch antenna, L-probe, differential feed, distributed MIMO, near field transformation, Butler Matrix

[1] *Ericsson Antenna Technology Germany GmbH, Rosenheim, Germany*
*__Corresponding authors__: duy.hai.nguyen@ericsson.com; martin.jacob@ericsson.com

Received: 23/05/2025, Accepted: 21/10/2025, Published: 28/11/2025

1. Introduction

The upcoming sixth-generation (6G) wireless communication standard is expected to significantly extend the capabilities of current mobile networks. It will involve not only the adoption of new spectrum but also the introduction of novel functionalities and network architectures, such as distributed MIMO. Consequently, the development of innovative antenna technologies will be essential. Balancing coverage and bandwidth, the cmWave frequency range ($7.125 - 24.25$ GHz) has emerged as a promising spectrum for future wireless communications [1, 2]. Both global and regional regulatory efforts have already begun preparing for effective integration and coexistence with existing services operating in this band [3, 4].

Applications within this new spectrum range from indoor network deployments to outdoor use cases. From an antenna design perspective, radiators must offer both wide bandwidth and scalability. To address these needs, this paper proposes a novel planar PCB-based antenna optimized for energy-efficient indoor campus network deployments, such as user-centric distributed MIMO (D-MIMO) systems [5]. In such networks, a large number of low-complexity antenna processing units (APUs) are distributed throughout the service area, enabling macro-diversity and reducing interference compared to traditional centralized massive MIMO (mMIMO) systems, as illustrated in Fig. 1. While the radiator is primarily designed for such D-MIMO systems, it is also suitable for other use cases, including conventional and massive MIMO base station antennas.

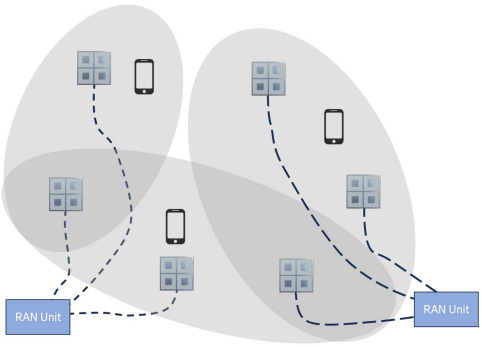

Figure 1: User centric D-MIMO architecture with 2x2 antenna arrays.

To achieve stable radiation characteristics and high port-to-port isolation, differential-fed radiators are commonly employed [6]. However, balanced excitation networks are often

complex and occupy significant space. To offer a simpler and more cost-effective solution, the proposed antenna uses L-shaped probes combined with out-of-phase delay lines. Shorting vias are added at the feed points to enhance out-of-band suppression. As a result, the antenna achieves dual polarization, stable radiation patterns, and excellent return loss (better than 13 dB) across the 12 to 14 GHz band. It also provides effective signal suppression in the current 5G NR mmWave band n258 (24.25 – 27.5 GHz) [7]. This consideration is important for mitigating interference between co-located cmWave and mmWave systems, whether at the same site or within the same housing.

Finally, measurement challenges related to connector induced radiation artifacts are addressed. A post-processing method based on equivalent current reconstruction is applied to isolate the true antenna radiation, enabling accurate validation of the beamforming behavior using a 4×4 Butler matrix. This comprehensive approach supports the proposed antenna's suitability for practical 6G deployments.

The remaining part of the paper is organized as follows. In section 2, the general antenna design and its radiating mechanism is presented; in section 3 the simulated antenna performance is shown; experimental verifications of the designs are discussed in section 4; and section 5 concludes the paper.

2. Antenna Design

2.1. Antenna technology

For a highly integrated antenna system, the design employs multilayer PCB technology. The general structure is illustrated in Fig. 2 and Fig. 3. The top layer contains a radiating patch, while the reflector is placed at layer 4 (L4), which also serves as a common ground plane for the excitation network located on the bottom layer. This configuration improves isolation between the radiating and feeding structures, allowing independent development and optimization of each. Key techniques used to reduce production costs include: (*a*) a sustainable, simplified multilayer PCB process, and (*b*) a capacitive, open-stub probe excitation method that requires minimal substrate thickness. For instance, high-performance yet cost-effective Megtron 7 laminates [8] are used for both the radiator layers (Top – L4) and the coplanar waveguide (CPWG) feeding network (L4 – Bottom), with respective thicknesses of 2.375 mm and 0.217 mm. Instead of using cost-intensive buried vias, the antenna cavity is implemented using plated-through holes (PTH), and the feeding probes and shorting pins are designed with sufficiently large diameters (0.4 mm) to allow direct drilling. To suppress surface wave propagation in the dielectric, the cavity height can

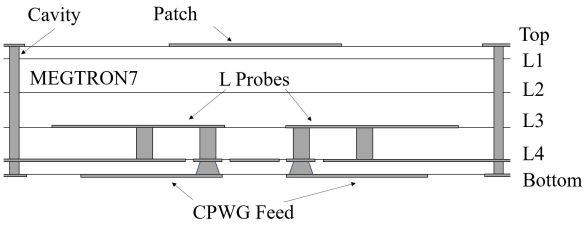

Figure 2: PCB layer stackup.

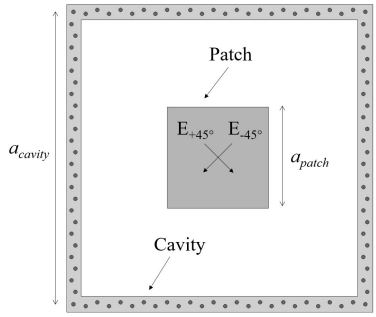

(a) Top.

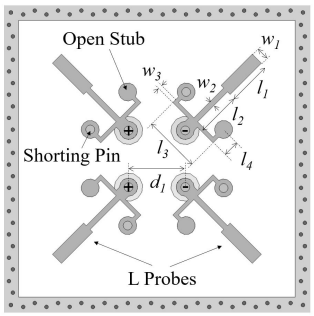

(b) L3.

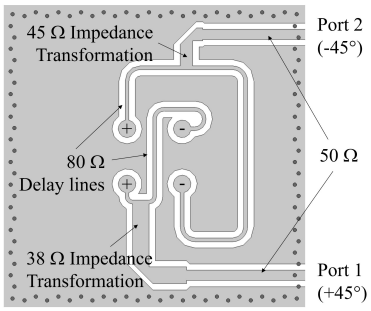

(c) Bottom.

Figure 3: Layout of the three functional layers of the antenna stackup.

be reduced to the L3 – Bottom layers [9], without significantly affecting input impedance matching. However, in this design, a full-height cavity is preferred to achieve a wider half-power beamwidth (HPBW) [6], which supports broader beam scanning coverage for indoor applications.

2.2. Radiating mechanism

This work adopts patch antennas due to their structural simplicity and ease of integration with PCB technology. As shown in Fig. 3a, a square patch is etched to provide symmetrical radiation characteristics for dual polarization. Slanted polarizations ($\pm 45^{o}$) are achieved by rotating the differential feeding pairs, implemented using L-shaped probes, as illustrated in Fig. 3b. To establish resonance within the desired frequency range, the dimensions of the radiating patch and feeding probes are tuned to approximately a quarter wavelength in the dielectric, enabling maximum coupling. However, a single resonance does not provide sufficient bandwidth. To extend it, a pair of open stubs

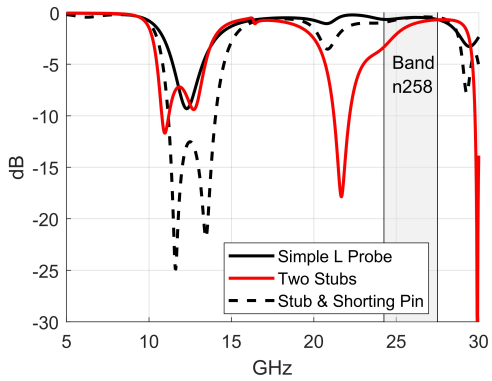

Figure 4: Differential input's impedance matching comparison (S_{d11}), marked by plus and minus signs in the Fig. 3b.

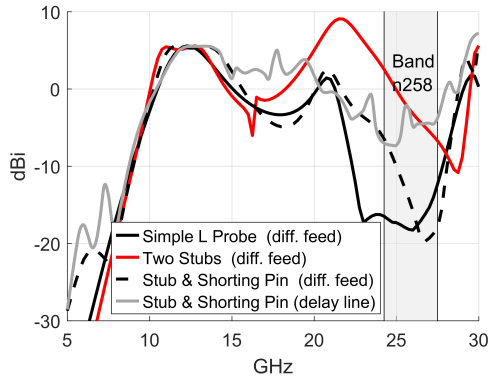

Figure 5: Simulated, realized gain of +45° slanted polarization at different design stages.

is introduced near the signal line vias, establishing a second resonance, as shown in Fig. 4. Due to coupling between the two resonant paths, the original patch resonance slightly shifts toward lower frequencies. Additionally, the stepped-impedance structure of the feeding probes improves impedance matching at the antenna input.

In addition to extending bandwidth, out-of-band signal rejection is also considered during antenna development. Modern communication systems use multiple frequency bands, and multiple antenna platforms are often co-located or integrated into a single base-station form factor to reduce footprint. This coexistence increases inter-band interference, which can significantly degrade RF performance. From the antenna front end, interference is mitigated when the radiators not only cover the desired band but also strongly suppress their response at other bands, providing high out-of-band rejection. Cross-band interference is assessed by analyzing the antenna's realized gain across the relevant frequency spectrum, as shown in Fig. 5. A negative realized gain indicates inefficient radiation and implies reduced electromagnetic coupling to undesired signals. According to the Fig. 5, while the symmetrical double open stubs effectively increase the impedance bandwidth, they also introduce unintended radiation around 21.6 GHz. This results in possible interference within the lower frequencies of band n258 (24.25–27.5 GHz). To mitigate this, shorting pins are added to one end of the double stubs, redirecting unwanted currents to ground. Due to the differential feeding configuration, these pins are placed symmetrically with respect to the antenna center (Fig. 3b). This configuration creates a radiation null near 26.5 GHz, where the gain becomes deeply negative. For instance, Fig. 6b shows the surface current distribution at 26.5 GHz for the +45° polarized port, with most of the current short-circuited at the pin locations. On the other hand, these shorting pins do not affect radiation at the intended frequency, as shown in Fig. 6a. As a result, the antenna preserves its gain within the target band while achieving strong suppression — ranging from 11.8 to 25.3 dB — across the n258 band, relative to the peak gain at 13.6 GHz. This enhanced cross-band isolation is also evident in Fig. 4, where the differential input reflection coefficient (S_{d11}) [10], marked by plus and minus signs in Fig. 3b, improves by approximately

Table 1: Single antenna element geometries.

Parameter	a_{patch}	a_{cavity}	l_1	l_2	w_1
Value (mm)	4.0	11.3	1.71	1.71	0.5
Parameter	w_2	l_3	w_3	l_4	d_3
Value (mm)	0.2	2.2	0.15	0.65	2.19

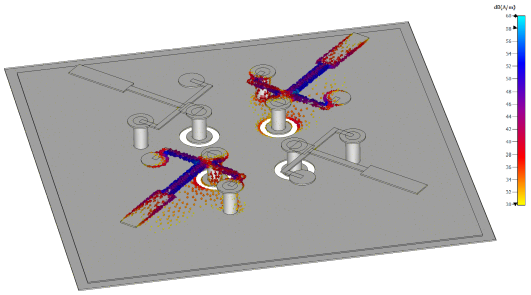

(a) Radiation condition at 13 GHz with optimum current distribution along the L probes.

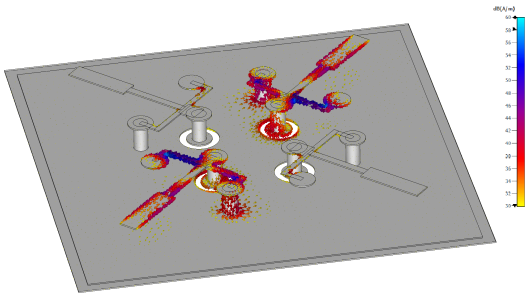

(b) Radiation rejection at 26.5 GHz due to current is short-circuited.

Figure 6: Simulated surface current distribution at 13 GHz (resonance) and 26.5 GHz (anti-resonance) for one polarization.

3 dB and approaches total reflection at 24.25 GHz after the shorting pins are added.

Finally, a simple power splitter with an out-of-phase transmission line is implemented on the bottom layer and connected to the differential feed pins, as shown in Fig. 3c. To further simplify the antenna structure within the available space, the differential input impedance (S_{d11}) is designed to match 80 Ω. This allows the narrow transmission lines and delay elements to be connected directly, minimizing the need for complex impedance transformation to achieve the final 50 Ω at the connector interface. The impact of the power splitter on realized gain is also shown in Fig. 5. Relative to ideal differential feeding, the gain is well maintained across the band of interest. Out-of-band rejection in the n258 band is reduced because the out-of-phase delay line is bandwidth-limited; this choice lowers cost and circuit complexity. Nevertheless, a minimum realized gain of −3 dBi is still achieved in the millimeter-wave spectrum.

3. Antenna Performance

Given the general radiation principles introduced in Section 2, this section presents the detailed antenna geometry and performance characteristics. The design is optimized for the 12 to 14 GHz frequency range and is intended for integration into antenna processing units (APUs) within industrial indoor D-MIMO networks (Fig. 1).

3.1. Single radiator optimized for 12-14 GHz

The antenna is developed and optimized for a target frequency range of 12 to 14 GHz using the 3D electromagnetic simulation tool CST. The resulting physical dimensions are summarized in Table 1.

Figure 7 shows the simulated results, including the impedance matching and the realized gain of the single radiator. A return loss of 10 dB or better has been achieved between 11.75 and 14.25 GHz (20 % relative bandwidth). This provides sufficient margin to accommodate frequency shifts caused by manufacturing tolerances. The radiating structure is highly symmetrical, except for the feeding network. For example, the delay lines are different for each polarization to enable implementation on a single PCB layer (Fig. 3c), resulting in slightly different return loss characteristics. The antenna ports maintain excellent isolation, better than 33 dB across the operating band.

In addition, the antenna provides a realized gain between 5.4 and 6 dBi, with a typical radiation efficiency of 92%. Horizontal and vertical radiation cuts are shown in Fig. 7. As illustrated, the antenna exhibits stable radiation characteristics over the whole frequency range with a wide half-power beamwidth (HPBW) of approximately 90°. The crosspolar discrimination in the main beam direction is better than 19 dB. Both making the array well-suited for efficient dual polarized beamforming in indoor environments.

3.2. Uniformly spaced 2x2 antenna array

A uniformly spaced 2×2 antenna array with center to center element spacing a_{cavity} in x and y direction, is selected as the radiating unit for the D-MIMO APU (Fig. 1). The top view is shown in Fig. 8. To enable wide-area coverage, we propose using low-complexity analog beamforming through phase shifters

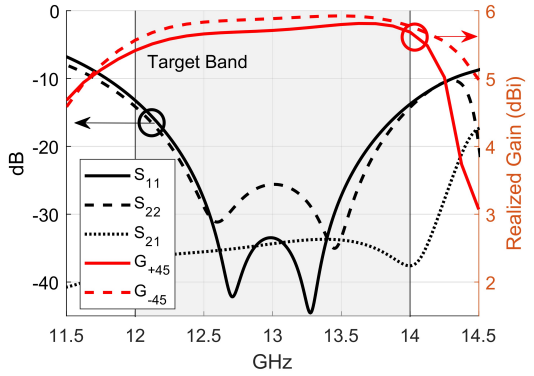

(a) Simulated S-parameters and realized gain.

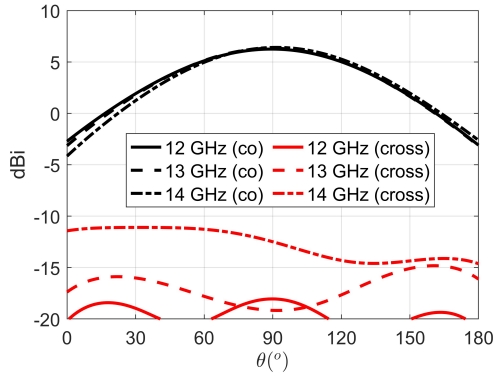

(b) Elevation Cuts.

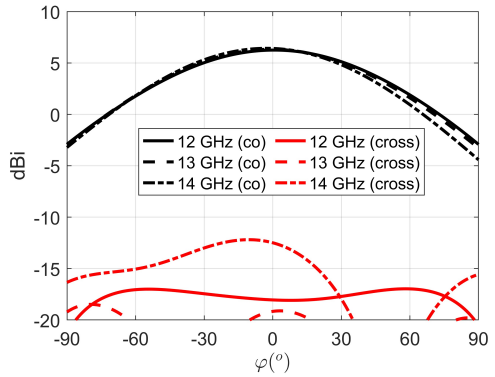

(c) Azimut Cuts.

Figure 7: Simulated S-Parameters and radiation pattern cuts (directivity) of the dual polarized single radiator.

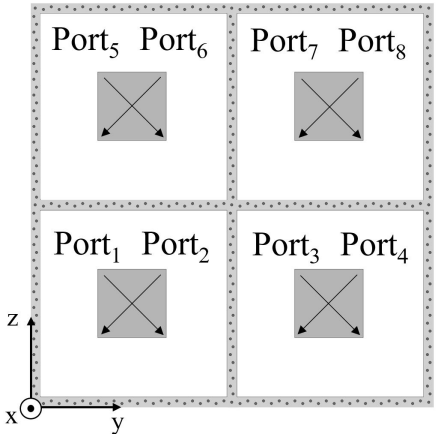

Figure 8: Top View of the 2×2 array configuration.

or Butler matrix distribution networks [11]. The increase of antenna directivity — approximately 6 dB compared to a single radiator — can significantly enhance the communication link budget while maintaining the low complexity of the proposed APU.

Figure 9 shows the simulated S-parameters of the four radiating elements in the array. Due to the array's symmetry, all elements exhibit similar behavior. Compared to the single radiator, the operating frequency band shifts slightly toward lower frequencies. Nonetheless, return losses above 13 dB are maintained. The mutual coupling between the $+45°$ polarization of port 1 and the other ports is illustrated in Fig. 9b. The isolation between orthogonal polarizations within the same element (S_{21}) remains above 33 dB, consistent with the single radiator. Coupling to adjacent elements is lower than -17 dB. For brevity and due to the array's symmetry, not all entries of the 8-port S-matrix are displayed.

By applying five different sets of phase weights (Table 2), beamsteering in both the elevation and azimuth planes enables wide spatial coverage, as demonstrated in Fig. 10. Three beam directions are shown, with the main lobe steered toward the center, left, and right in the horizontal plane. It is important to note that ideal phase weights are assumed, no additional losses or frequency-dependent effects are considered. Therefore, directivity is discussed instead of realized gain. The boresight beam exhibits a half-power beamwidth (HPBW) of 48° and a maximum directivity of 11.2 dBi, with side lobe suppression better than 13 dB. When using a 90° phase shift, the beam is steered to $\varphi = \pm 22°$ with a maximum directivity of 10 dBi. In these cases, side lobes appear at $\varphi = \pm 58°$ with suppression of approximately 5 dB. The HPBW envelope of the three beam patterns is 80°, which is slightly narrower than that of the single element, as expected due to array scan loss. The scanning behavior in the elevation plane is similar due to the array's symmetry and is omitted here for brevity. The codebook can easily be realized either in the digital domain or with analog circuits. An example realization will be presented in Sec. 4.3.1.

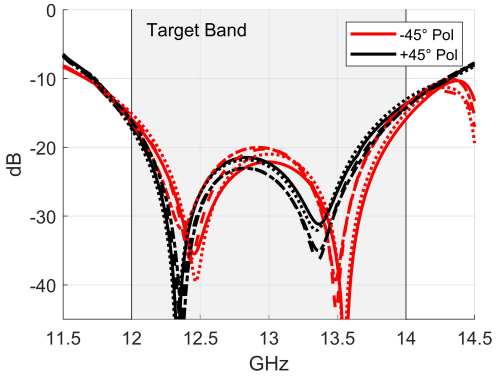

(a) Reflection coefficients.

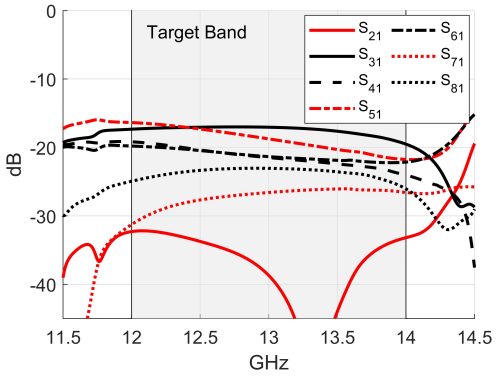

(b) Example mutual coupling coefficients for port 1.

Figure 9: Simulated element S-Parameters of the uniformly spaced 2x2 array configuration.

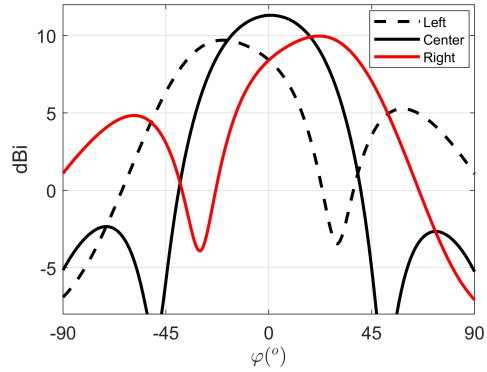

Figure 10: Radiation pattern cuts at 14 GHz of the 2x2 array configuration for +45° polarization. Three exemplary beams are shown steered to boresight, to the left and to the right .

Table 2: Phase weight codebook.

Beam:	Center	Left	Right	Up	Down
$\text{Port}_{1/2}$	0°	0°	90°	0°	90°
$\text{Port}_{3/4}$	0°	90°	0°	0°	90°
$\text{Port}_{5/6}$	0°	0°	90°	90°	0°
$\text{Port}_{7/8}$	0°	90°	0°	90°	0°

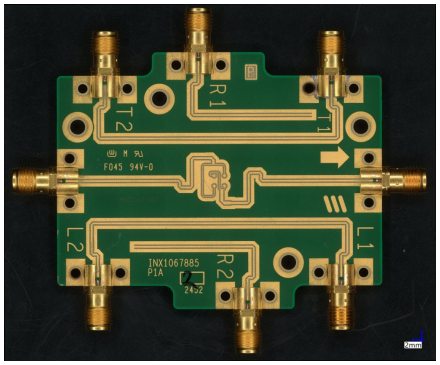

Figure 11: Bottom view of the manufactured single radiator. TRL calibration kit is also included

4. Experimental Verification

The proposed antenna designs were fabricated and validated through measurements. This includes evaluation of their radiation characteristics in a compact antenna test range. This section presents the performance results of both a single radiator (Sec. 4.1) and a 2×2 antenna array. The array is measured port-wise (eight ports) (cf. Sec. 4.2). In addition beamforming with a 4×4 Butler matrix is demonstrated.

4.1. Single radiator

Fig. 11 shows a bottom-view photograph of the fabricated antenna. As shown in the figure, in addition to the radiator structure, a Through-Reflect-Line (TRL) calibration kit [12] is included. This allows the effects of the coaxial connector and its transition to be excluded from the measurements. As a result, the experimental data can be directly compared with the simulation results at the same reference plane, as shown in Fig. 3c. To achieve the required bandwidth, in addition to the through line, a single transmission line with a quarter-wavelength at the center frequency (13 GHz) is sufficient for effective calibration coverage. Ideally, the coaxial-to-cpwg transitions in the calibration kit and the antenna ports would have the same geometry. However, the TRL kit uses a different transition design intended for characterizing other RF components, which are beyond the scope of this paper. Nevertheless, the electrical phase delay introduced by these transitions is identical.

The measured scattering parameters and radiation patterns of the single radiator, shown in the horizontal and vertical cuts, are presented in Fig. 12, respectively. Good agreement between measurements and simulations is observed. For example, the antenna exhibits an impedance bandwidth of approximately 2 GHz for a reflection coefficient below -13 dB. The isolation between the dual-polarized ports exceeds 25 dB. A slight downward frequency shift in the operating band is recorded, which may be attributed to higher dielectric constants in the laminate materials. Furthermore, the measured radiation gains at 13 GHz closely match the simulations in both planes. The deviations compared to the ideal radiation patterns (Figure 7) can be attributed to the larger ground plane and the impact of connectors and cables during experimental verification. Similar trends are observed at the other port and at other frequencies, but these results are not shown here for brevity.

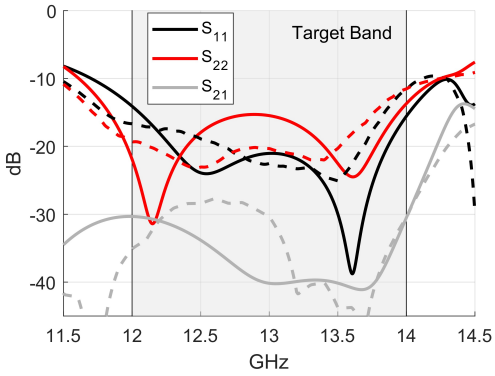

(a) S-parameters.

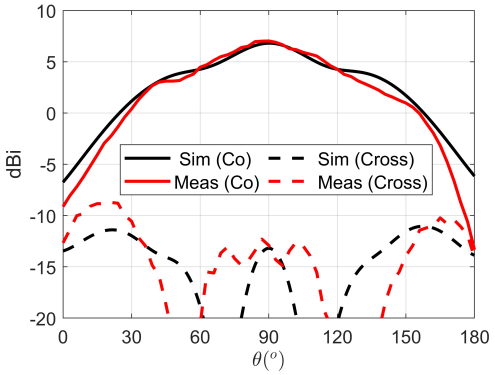

(b) Elevation cut

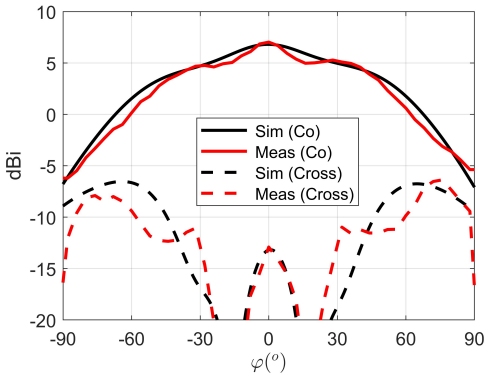

(c) Azimuth cut

Figure 12: Measured and simulated S-Parameters as well as radiation cuts (realized gain) of the single antenna.

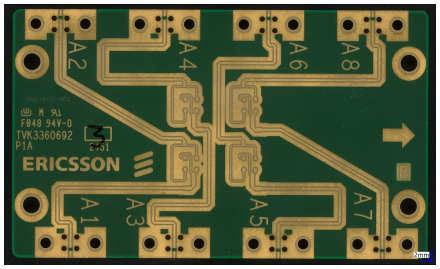

Figure 13: Bottom view of manufactured 2×2 antenna array.

4.2. 2×2 antenna array

Fig. 13 depicts the bottom view of the manufactured 2×2 antenna array before soldering the SMA connectors. For a top view of the array we refer to Fig. 17. The transmission lines are designed for the same electrical length. This allows convenient operation with external beamforming networks like phase shifters or Butler matrices which will be discussed further in Sec.4.3. In the following the characteristics of the 2×2 antenna array are presented. This includes TRL calibrated deembeded S-Parameters and radiation patterns including a comprison between measurements and 3D electromagnetic simulations.

Given the array's high degree of symmetry, only the S-parameters of port A1 (i.e., $+45^\circ$ polarization) are shown in Fig. 14a; the other ports exhibit nearly identical behavior. The reflection coefficient at this port follows the trend observed for the single radiator in the previous section. Port isolation remains above 25 dB between the two polarizations of the same element and exceeds 17 dB between adjacent elements.

The horizontal and vertical radiation cuts from the selected port are shown for the center frequency in Fig. 14. The experimental results for the single radiator and the 2×2 array show good agreements with simulation for both the co- and cross-polarized field. However, some significant ripples appear in the measurements, which cannot be fully explained by manufacturing tolerance or environmental reflections. In order to investigate this behavior, a detailed geometric model was used for comparison to the measurements (cf. Fig. 18). As seen in the figure, the connectors and load terminals are relatively large compared to the wavelength at the operating frequency and are located close to the antenna array. This makes them potential sources of scattering that can affect the radiation pattern. This could be confirmed by comparing the more detailed model's results with the results of Sec. 3. These results suggest that the placement of coaxial connectors near the array influences the radiation characteristics. However, within the intended application, this effect would not occur when the antenna is fully integrated into the APU, where external connectors are not required. In addition, we present a post-processing method to spatially filter out this kind of influences in Sec. 4.3.2.

4.3. 2×2 antenna array beamforming performance

To demonstrate the beamforming capabilities of the proposed antenna array, a 4×4 Butler matrix was designed and tested. The matrix provides fixed analog beam steering for the 2×2 dual-polarized antenna array, enabling low-complexity directional coverage and signal-to-noise ratio enhancement. The

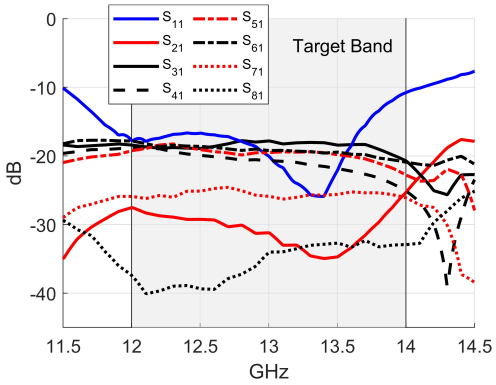

(a) Measured S-parameters of the antenna array for port A1.

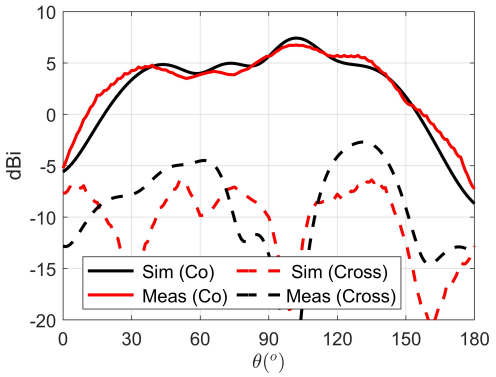

(b) Elevation cut.

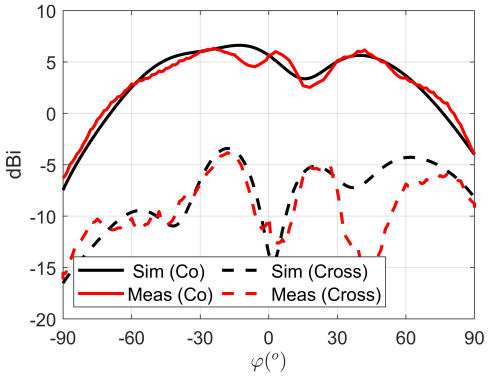

(c) Azimuth cut.

Figure 14: Measured and simulated S-Parameters as well as radiation cuts (realized gain) of the antenna port A1.

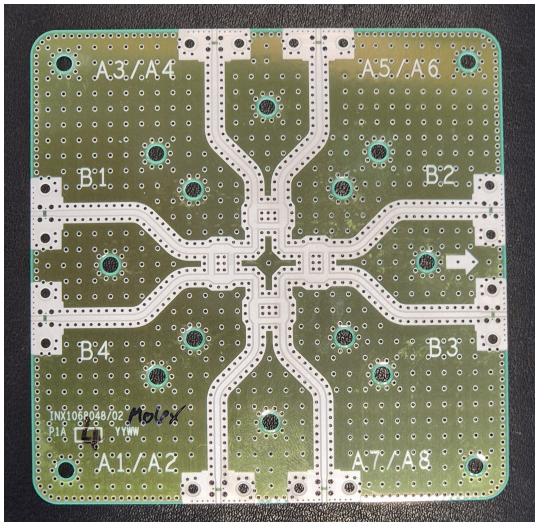

Figure 15: 4×4 Butler Matrix.

beamforming evaluation consists of two parts. First, the design and measured performance of the Butler matrix are presented in Section 4.3.1. Then, in Section 4.3.2, the radiation patterns of the combined array and Butler matrix are examined, using post-processing to remove measurement artifacts and isolate the true antenna response.

4.3.1. 4×4 Butler Matrix

The fabricated 4×4 Butler matrix is shown in Fig. 15. It is built on a dual-layer PCB using glass-reinforced ceramic laminate and employs CPWG transmission lines for compact routing and low loss. The matrix consists of four identical 90° hybrid couplers, interconnected to form a complete Butler circuit that feeds the 2×2 antenna array.

Each input port of the Butler matrix (B1–B4) excites the antenna elements (A1–A4) with specific amplitude and phase combinations, generating four directional beams spaced at fixed angles. For example, when port B1 is excited, the diagonal antenna elements receive the same phase, while the opposite diagonal pair receives a $\pm 90°$ phase shift, creating a tilted beam. This enables simple, hardware-efficient beam steering without the need for digital processing or variable phase shifters.

Fig. 16 shows the measured amplitude and phase differences for one input port (B1), relative to a reference antenna port (A1). Amplitude variations are within ± 0.7 dB, and phase errors are minimal across frequency range of interest. These results confirm the Butler matrix performs as expected over the antenna's operating bandwidth, supporting consistent and predictable beam steering behavior.

4.3.2. Radiation Ripples and Spatial Filtration

In practical measurement environments, it is difficult to completely avoid the influence of nearby objects such as connectors, cables, and mounting hardware. These elements can introduce unwanted reflections and radiation, especially when they are located close to the antenna under test (AUT). This is particularly relevant in our measurements, where SMA connectors and load terminations near the 2×2 array were found to produce noticeable ripples in the radiation pattern.

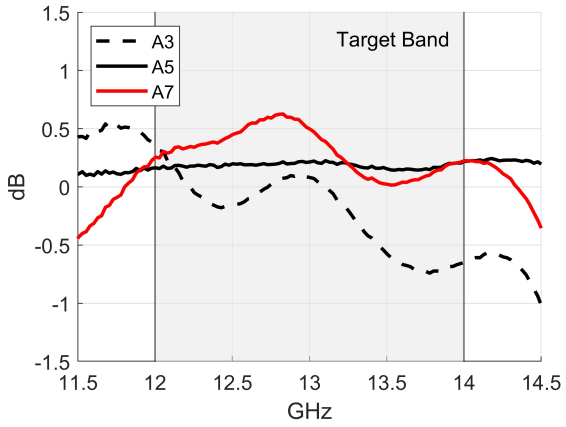

(a) Amplitude deviation.

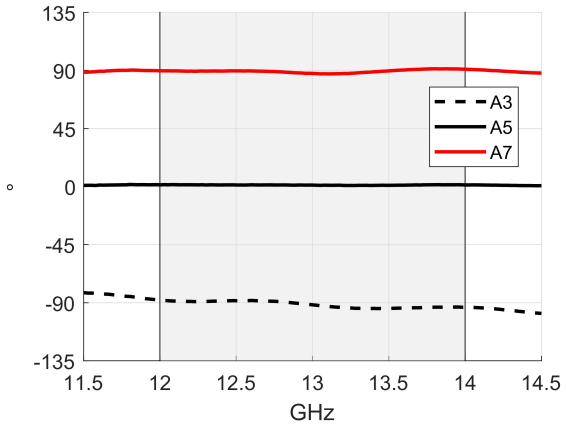

(b) Phase Difference

Figure 16: Amplitude and phase differences for beam port B1. Reference amplitude and phase measured at port A1.

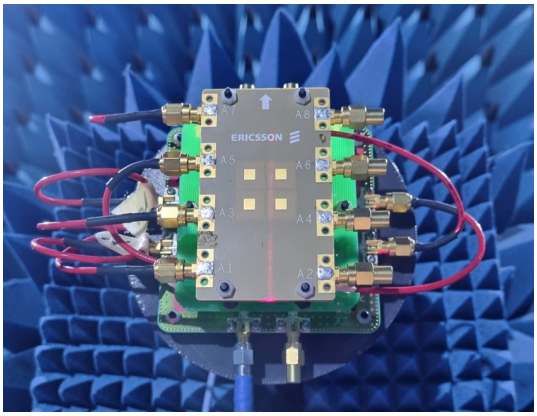

Figure 17: Measurement setup for the 2×2 antenna array connected to the Butler Matrix located behind.

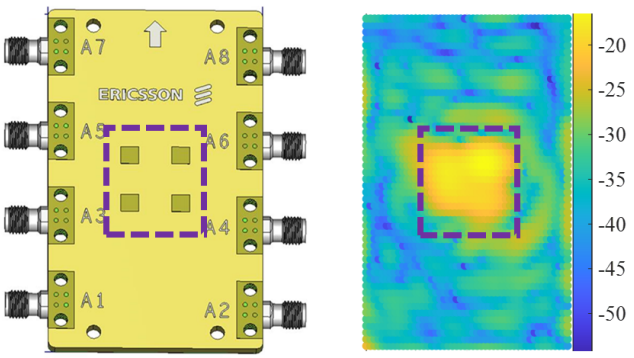

Figure 18: Equivalent currents derived by inverse transformation of complex far field data.

To address this, a spatial filtering technique was applied to extract the actual antenna radiation. The process uses an advanced near-field to far-field transformation algorithm [13], applied in the Compact Antenna Test Range (CATR) setup:

- A square Huygens surface is defined above the array (see Fig. 18).
- The measured far-field is inverse-transformed into equivalent electric current densities on this surface, capturing the radiation sources.
- Only the currents confined to the antenna aperture are retained. Currents from parasitic sources (e.g., connectors) are excluded.
- These filtered currents are then forward-transformed to obtain a clean far-field radiation pattern.

Fig. 18 shows the antenna array layout and the equivalent currents, plotted on a logarithmic scale, on a Huygens' surface that coincides with the top layer of the antenna. These currents are obtained by applying an inverse transform to the measured far-field data. A 5 cm $\times$ 5 cm window encloses the dominant radiating region and is used to reconstruct the corresponding far fields from the measurements. The window size generally depends on the antenna geometry and aperture. For this antenna, it is chosen to retain the most relevant radiated fields while sufficiently suppressing unwanted distortion. Fig. 19 illustrates the effectiveness of the spatial filtering method by comparing simulated and measured radiation patterns before and after filtering. After applying spatial filtering, the measured patterns closely match the simulations. Hence, this step is critical for reliable validation of the antenna's beamforming performance, especially when external connectors are not part of the intended end-use scenario. In deed, a comparison in radiation pattern cuts between simulation and measurement of the 2×2 antenna array connected to the 4×4 Butler matrix were evaluated in Fig. 20. The results show an excellent match in beam direction and shape, confirming the accuracy of both the design and the measurement approach.

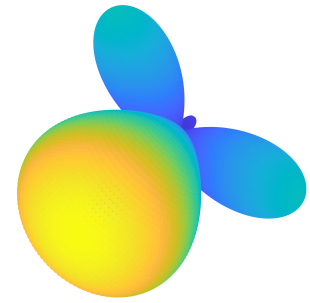

(a) Simulation.

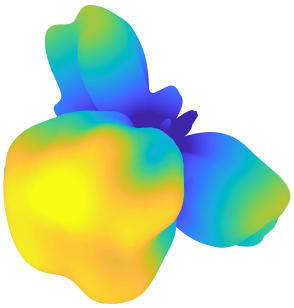

(b) Measured raw data.

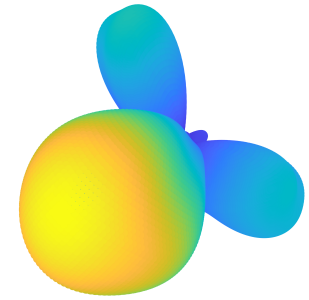

(c) Filtered measurement data.

Figure 19: Beam generated by 2×2 antenna array connected to the 4×4 Butler matrix shown in Fig. 15.

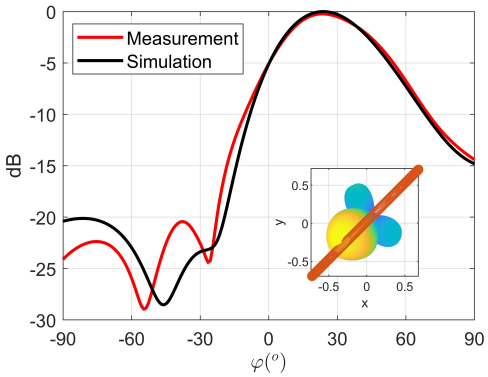

Figure 20: Pattern comparison of filtered FF cuts from CATR measurements and 2×2 array simulation at 14 GHz. The inset shows the cut-plane from $+z-$ direction.

5. Conclusion

In this paper, a planar dual-polarized filtering antenna was presented for operation in the cmWave frequency range. A multilayer PCB process was employed to provide a cost-effective solution suitable for integration into future 6G hardware. The single antenna elements achieve realized gains between 5.4 and 6 dBi with a typical radiation efficiency of 92% across a 2 GHz bandwidth centered at 13 GHz. Out-of-band suppression is achieved directly within the radiating structure, enabling mitigation of potential interference with the 3GPP mmWave band n258. These excellent characteristics are achieved through a simple differential L-probe feed integrated with additional shorting pins. A uniformly spaced 2×2 phased array was also evaluated, demonstrating the technology's potential for D-MIMO applications.

Acknowledgment

This work was partially funded by the German Federal Ministry of Research, Technology and Space (BMFTR) within the research project Cell Free Massive MIMO Systems - MassIMO, funding label 16*KISK*073.

References

[1] M. V. Katwe, A. Kaushik, K. Singh, M. Di Renzo, S. Sun, D. Lee, A. G. Armada, Y. C. Eldar, O. A. Dobre, and T. S. Rappaport, "cmWave and Sub-THz: Key Radio Enablers and Complementary Spectrum for 6G," *arXiv preprint arXiv:2406.18391*, 2024.

[2] "Study on the 7 to 24 GHz frequency range for NR," The 3rd Generation Partnership Project, Tech. Rep. TR 38.820 V16.1.0 (2021-04), 2021.

[3] "World Radiocommunication Conference 2023 (WRC23) Final Acts," "International Telecommuniction Union (ITU-R)", Tech. Rep., 2023, www.itu.int/dms_pub/itu-r/opb/act/R-ACT-WRC.16-2024-PDF-E.pdf.

[4] "A Preliminary View of Spectrum Bands in the 7.125 - 24 GHz Range; and a Summary of Spectrum Sharing Frameworks," Federal Communications Commission, Tech. Rep., 2023.

[5] G. Interdonato, E. Björnson, H. Quoc Ngo, P. Frenger, and E. G. Larsson, "Ubiquitous cell-free massive mimo communications," *EURASIP Journal on Wireless Communications and Networking*, vol. 2019, no. 1, pp. 1–13, 2019.

[6] C. A. Balanis, *Antenna Theory: Analysis and Design*, 2nd ed. John Wiley Sons, 1997.

[7] "User Equipment (UE) radio transmission and reception," The 3rd Generation Partnership Project, Tech. Rep. TS 38.101-1 V18.7.0 (2024-010), 2023.

[8] *High Speed Low Loss Multi-layer Materials*, Panasonic Industry, 2022.

[9] R. Garg, P. Bhartia, I. Bahl, and A. Ittipiboon, *Microstrip Antenna Design Handbook*. Artech House, 2001.

[10] D. M. Pozar, *Microwave engineering; 3rd ed.* Hoboken, NJ: Wiley, 2005. [Online]. Available: https://cds.cern.ch/record/882338

[11] M. M. M. Ali and A.-R. Sebak, "2-D Scanning Magneto-electric Dipole Antenna Array Fed by RGW Butler Matrix," *IEEE Transactions on Antennas and Propagation*, vol. 66, no. 11, pp. 6313–6321, 2018.

[12] G. Engen and C. Hoer, "Thru-reflect-line: An improved technique for calibrating the dual six-port automatic network analyzer," *IEEE Transactions on Microwave Theory and Techniques*, vol. 27, no. 12, pp. 987–993, 1979.

[13] M. S. Castaner and L. J. Foged, *Post-processing Techniques in Antenna Measurement*. SciTech Publishing, 2019.